## Supporting information

# Wafer-scale two-dimensional platinum monosulfide ultrathin film via metal sulfurization for high performance photoelectronics

Jinbo Pang,#* Yanhao Wang,# Xiaoxin Yang,# Lei Zhang,# Yufen Li, Yu Zhang, Jiali Yang, Feng Yang,* Xiao Wang,* Gianaurelio Cuniberti□, Hong Liu, Mark H Rümmeli □□□□□□□□□□□□□□□□□□□□□□□□□□□□

Prof Jinbo Pang, Prof Hong Liu, Yufen Li, Jiali Yang
Collaborative Innovation Center of Technology and Equipment for Biological Diagnosis and Therapy in Universities of Shandong, Institute for Advanced Interdisciplinary Research (iAIR), University of Jinan, Shandong, Jinan 250022, China
Email: ifc_pangjb@ujn.edu.cn or jinbo.pang@hotmail.com

Yanhao Wang, Prof Yu Zhang
Institute of Marine Science and Technology, Shandong University, Shandong, Qingdao 266237, China

Yanhao Wang
The Interdisciplinary Research Center, Shanghai Advanced Research Institute, Chinese Academy of Sciences, 99 Haike Road, Zhangjiang Hi-Tech Park, Pudong, Shanghai 201210, China
School of microelectronics, University of Chinese Academy of Sciences, 19 Yuquan Road, Beijing 100049, China

Xiaoxin Yang, Prof. Xiao Wang
Shenzhen Key Laboratory of Nanobiomechanics, Shenzhen Institute of Advanced Technology, Chinese Academy of Sciences, Shenzhen 518055, China
Email: xiao.wang@siat.ac.cn

Dr Lei Zhang, Prof Feng Yang
Department of Chemistry, Guangdong Provincial Key Laboratory of Catalysis, Southern University of Science and Technology, Shenzhen 518055, China
Email: yangf3@sustech.edu.cn

Prof Dr Gianaurelio Cuniberti
Institute for Materials Science and Max Bergmann Center of Biomaterials, TU Dresden, Dresden 01069, Germany
Center for Advancing Electronics Dresden, TU Dresden, Dresden 01069, Germany

Prof Hong Liu
State Key Laboratory of Crystal Materials, Center of Bio & Micro/Nano Functional Materials, Shandong University, 27 Shandanan Road, Jinan 250100, China
E-mail: hongliu@sdu.edu.cn

Prof Mark H Rümmeli□□□
College of Energy, Soochow Institute for Energy and Materials Innovations, Soochow University, Suzhou 215006, China, Key Laboratory of Advanced Carbon Materials and Wearable Energy Technologies of Jiangsu Province, Soochow University, Suzhou 215006, China
Centre of Polymer and Carbon Materials, Polish Academy of Sciences, M. Curie Sklodowskiej 34, Zabrze 41-819, Poland
Institute for Complex Materials, IFW Dresden, 20 Helmholtz Strasse, Dresden 01069, Germany
Institute of Environmental Technology, VŠB-Technical University of Ostrava, 17. listopadu 15, Ostrava 708 33, Czech Republic

Prof Gianaurelio Cuniberti
Dresden Center for Computational Materials Science, Technische Universität Dresden, Dresden 01062, Germany
The Dresden Center for Intelligent Materials (DCIM), Technische Universität Dresden, Dresden 01062, Germany

*Corresponding authors.
E-mail: (J.P.) ifc_pangjb@ujn.edu.cn; (F.Y.) yangf3@sustech.edu.cn; (X.W.) xiao.wang@siat.ac.cn; (H. L.) hongliu@sdu.edu.cn;

#These authors contributed equally to this work.

## 1. Experimental details.

**Experimental details for HAADF-STEM image simulation.** HAADF-STEM image simulations of PtS [001] were performed using the Quantitative STEM (QSTEM) simulation package. The simulations were carried out using an 80 × 80 pixel area and a probe array of 400 × 400 pixel area with a specimen thickness of 10 to 12 nm. The microscope parameters used for the simulations were the same as those for imaging.

**Method for collecting the SAED data.** The low-magnification TEM imaging and electron diffraction of PtS film were performed on a FEI Tecnai F30 operated at 200 kV.

**Method for obtaining the average grain size.** The grain size was determined by averaging the length and the width for each grain by color mapping. This idea was inspired by the relative rotation angle between two adjacent graphene facets with the mapping by dark-field TEM and SAED approach.[1-3] Indeed, we have developed this SAED approach for determine the average grain size of 2D materials, as reported by our research team.[4] Besides, the grain size matches well with the aperture size from SAED data. Indeed, under electron-beam irradiation by the aperture size (ca. 220 nm), two sets of diffraction patterns emerge. And for a larger aperture size (ca. 860 nm), twelve sets of diffraction patterns were observed in SAED data. Therefore, the grain size was determined in a range from 220 nm to 290 nm. The number of grains inside the aperture was estimated from SAED patterns.

**Method for acquiring the device parameters of the photodetectors**. The rise time of the photodetector was determined by the time consumed for net photocurrent increasing from 10% to 90% upon illumination.[5, 6] The decay time of the photodetector was extracted by the time used by the net photocurrent decreasing from 90% to 10% upon the termination of illumination.[7, 8] The photodetection performance was evaluated in terms of responsivity (R), detectivity (D*), and response time (τ) in the device section. The responsivity was calculated by the expression.

$$R = I_{ph}/PS \tag{1}$$

in which $I_{ph}$ is the photocurrent, P is the per-unit power of the laser, and S is the effective area of the photodetector. And the detectivity is obtained as follows.

$$D^* = {R\sqrt{S}}/{\sqrt{2eI_d}} \tag{2}$$

in which *e* and $I_d$ is the electron charge and the dark current, respectively.

**More experimental details for DFT Computations.**

First principles calculations were performed using density-functional theory as implemented in the Vienna ab initio simulation package (VASP).[9, 10] A generalized gradient approximation (GGA) formulated by Perdew, Burke, and Ernzerhof (PBE) was chosen to describe the exchange-correlation.[11] Projector augmented wave (PAW) potentials were used in all calculations with a kinetic cutoff energy set as 300 eV.[12, 13] The Brilliouin zone is sampled in the Monhkorst-Pack scheme and a 18 × 18 × 1 k-point mesh was generated.[14] All the ionic relaxations in PtS and $PtS_2$ crystal structures were optimized by the recommended conjugate-gradient algorithm until the maximum atomic force component acting on each atom is less than 0.01 eV/Å. The thermodynamic phase diagram explored by comparing the difference of the Gibbs free energy $\Delta G$ between PtS and $PtS_2$ as follows:

$$\Delta G = G_{PtS_2} - G_{PtS} - N_s\mu_s \tag{1}$$

*Temperature-pressure dependent Gibbs free energy*: The Gibbs free energy *G* at pressure *P* and temperature *T* can be calculated as

$$G(P,T) = F_{phonon} + PV \tag{2}$$

In which $F_{phonon}$ is the phonon contribution to the Helmholtz free energy, *P* and *V* are the volume and pressure. Under quasi-harmonic approximation, the Helmholtz energy $F_{phonon}$ is given by

$$F_{phonon} = \frac{1}{2}\sum_{\boldsymbol{q},v}\hbar\omega_{\boldsymbol{q},v} + k_BT\sum_{\boldsymbol{q},v}\ln[1-\exp(\frac{-\hbar\omega_{\boldsymbol{q},v}}{k_BT})] \tag{3}$$

Where **q** and $v$ are the wave vector and band index, respectively, $\omega_{q,v}$ is the phonon frequency at **q** and $v$, and *T* is the temperature. $k_B$ and $\hbar$ are the Boltzmann constant and reduced Planck constant, respectively.

*The chemical potential of sulfur.* The chemical potential of sulfur as the functions of *T* and *P* can be written as[15]

$$\mu_S(T,P) = \frac{1}{2}\mu_{S_2} = \frac{1}{2}[E_{S_2} + E_{S_2}^{vib}(0K) + \Delta H(T,P^0) - T\Delta S(T,P^0) + k_B T \ln(\frac{p}{p^0})] \quad (4)$$

$E_{S_2}$ is the calculated energy of an isolated $S_2$ molecule and $E_{S_2}^{vib}(0K)$ corresponds to zero-point vibrational energy, also obtained from the calculations, $p$ is the partial pressure of sulfur and $p^0$ is the standard pressure as$10^5$ Pa. Both the change in enthalpy and the change in the entropy of $S_2$ are extracted from the thermochemical tables[16] at $p^0 = 10^5$ Pa.

## 2. Characterization of PtS and related materials.

### (1) Wafer-scale synthesis of PtS film with metal sulfurization approach

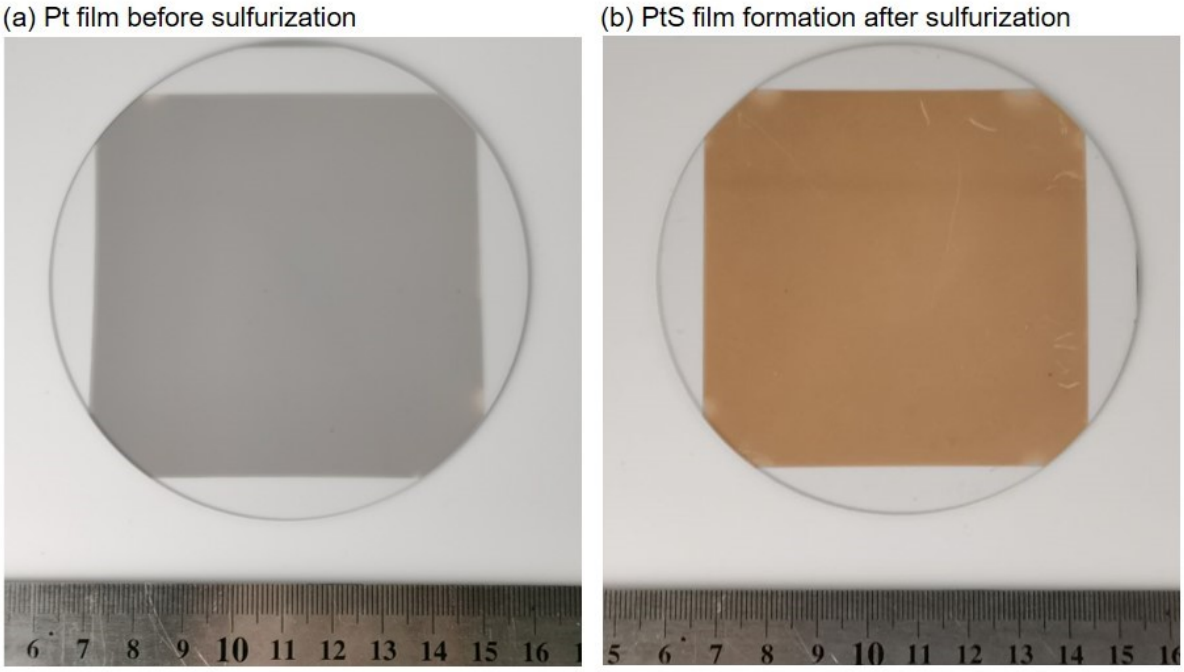


**Fig. S1** Wafer scale formation of PtS film via direct sulfurization approach. (a) Pristine Pt film over 4-inch quartz substrate. (b) PtS film formed over quartz after sulfurization. The thickness of pristine Pt film was 5 nm.

**(2) STEM and atomic resolution STEM for determining crystal structure**

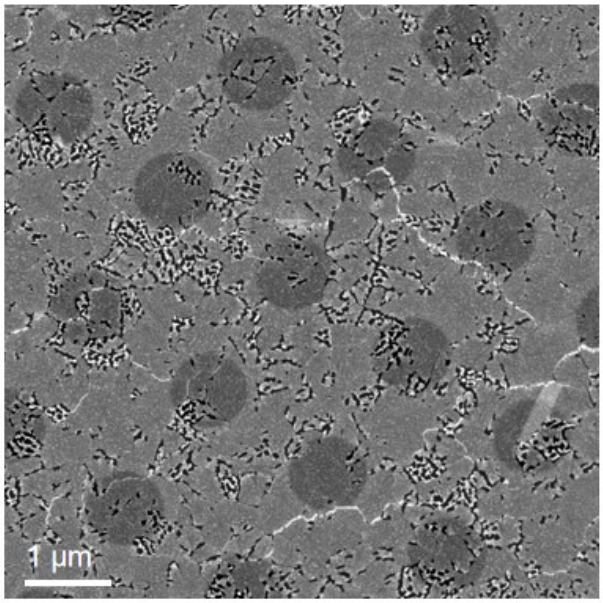


**Fig. S2**. A low-magnification HAADF-STEM image of the PtS thin film. The PtS was transferred onto a TEM grid (model: Quantifoil) with holes over carbon film.

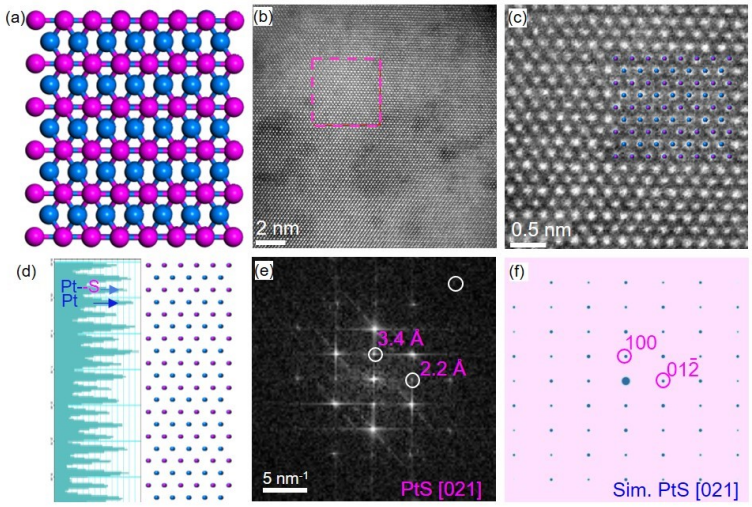


**Fig. S3**. The high-resolution STEM imaging of PtS along [021] axis. (a) Atomic configuration of PtS. (b) Low magnification and (c) atomic-resolution STEM images of PtS. (d) Intensity profile of a representative line across both Pt and S atoms. The line profile was drawn from the panel (c). (e) The fast Fourier transform result of the image in panel (c). (f) Simulated electron diffraction pattern of PtS [021] axis.

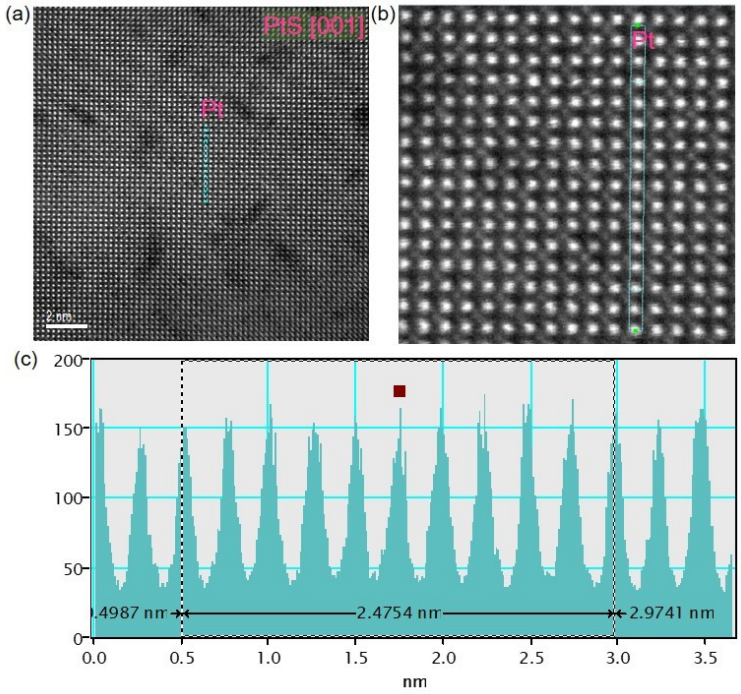


**Fig. S4** The determination of Pt-Pt distance along PtS [001] axis. (a) The line across the Pt atoms along PtS [001] axis. (b) The magnified image in panel (a). (c) The intensity profile of the line across the Pt atoms. The Pt-Pt has a distance of 0.25 nm.

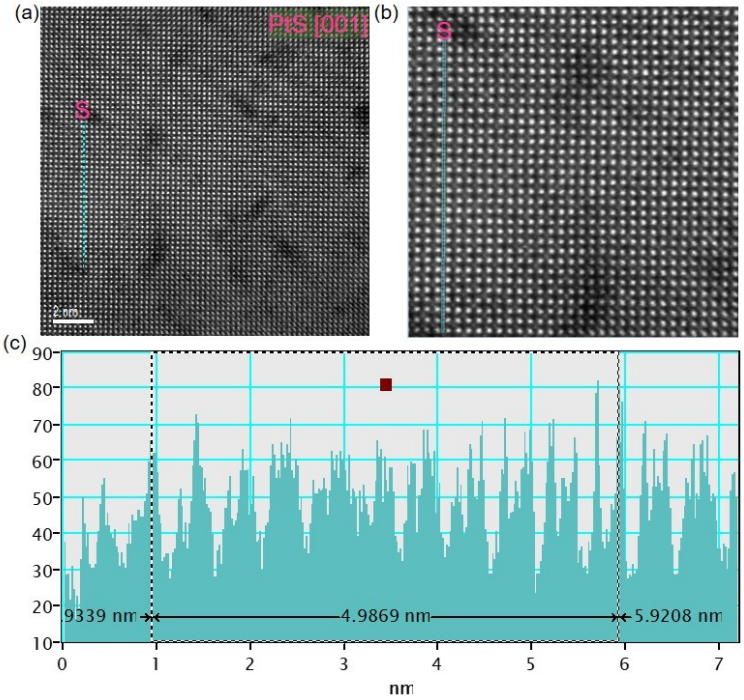


**Fig. S5** The determination of S-S distance along PtS [001] axis. (a) The vertical line across the S atoms along PtS [001] axis. (b) The magnified image in panel (a). (c) The

intensity profile of the line across the S atoms. The S-S has a distance of 0.5 nm.

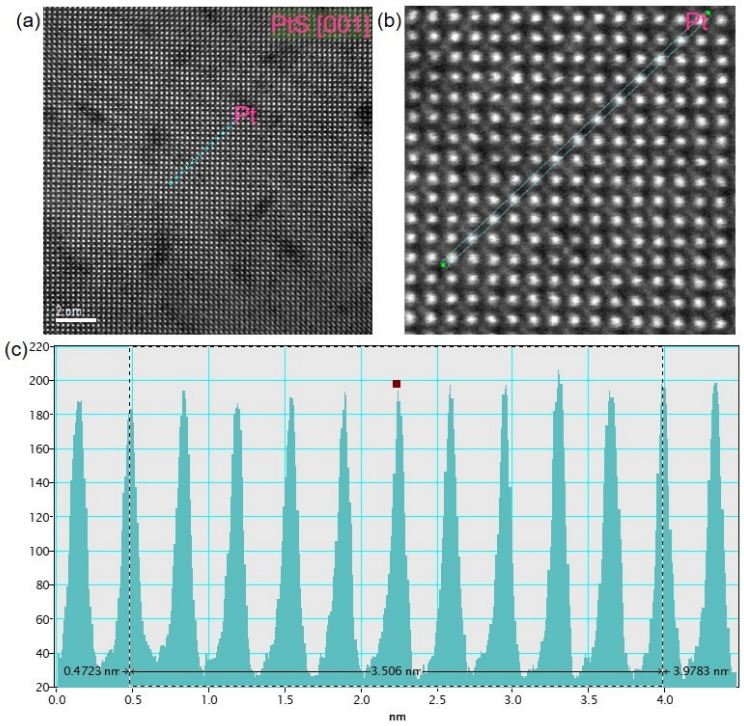


**Fig. S6** The determination of Pt-Pt distance along PtS [001] axis. (a) The diagonal line across the Pt atoms along PtS [001] axis. (b) The magnified image in panel (a). (c) The intensity profile of the diagonal line across the Pt atoms. The Pt-Pt has a distance of 0.35 nm.

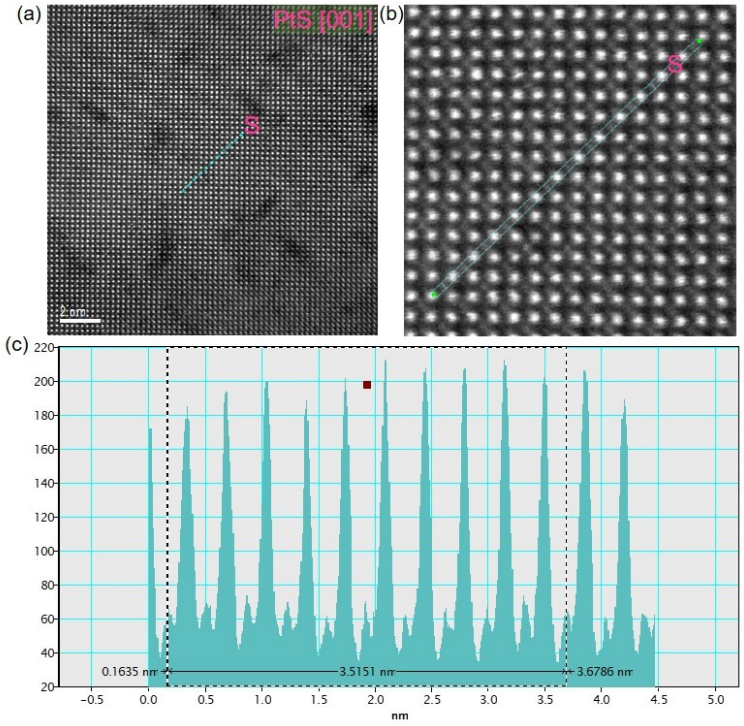


**Fig. S7** The determination of S-S distance along PtS [001] axis. (a) The diagonal line across the S atoms along PtS [001] axis. (b) The magnified image in panel (a). (c) The intensity profile of the diagonal line across the S atoms. The S-S has a distance of

0.35 nm.

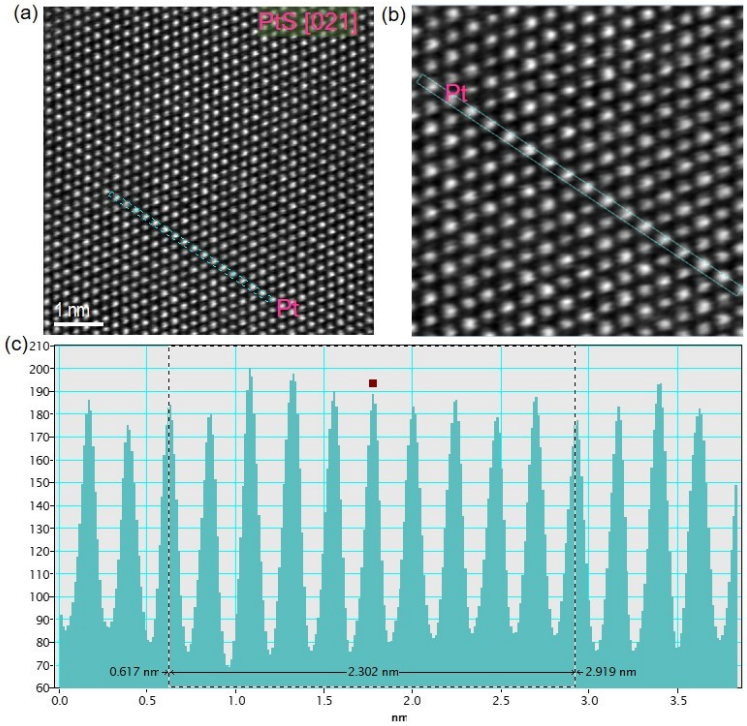


**Fig. S8** The determination of Pt-Pt distance along PtS [021] axis. (a) The line across the Pt atoms along PtS [021] axis. (b) The magnified image in panel (a). (c) The intensity profile of the line across the Pt atoms. The Pt-Pt has a distance of 0.23 nm.

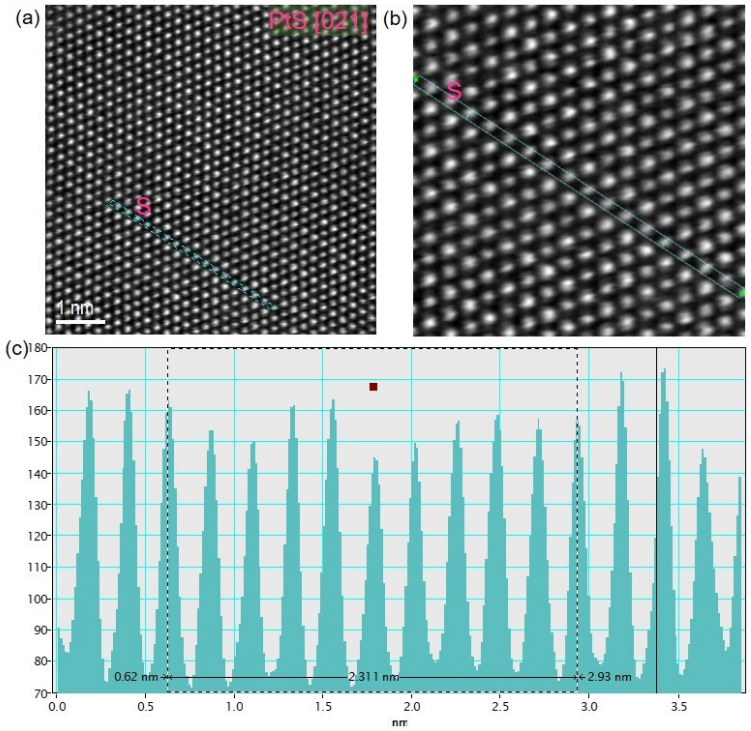


**Fig. S9** The determination of S-S distance along PtS [021] axis. (a) The line across the S atoms along PtS [021] axis. (b) The magnified image in panel (a). (c) The intensity profile of the line across the S atoms. The S-S has a distance of 0.23 nm.

**(3) SAED and STEM characterization for obtaining average grain size of the synthetic PtS film.**

**Method for obtaining the average grain size.** The grain size was determined by averaging the length and the width for each grain by color mapping. Besides, the grain size matches well with the aperture size from SAED data (**Fig. S10**a,b). Indeed, under electron-beam irradiation by the aperture size (ca. 220 nm), two sets of diffraction patterns emerge. And for a larger aperture size (ca. 860 nm), twelve sets of diffraction patterns were observed in SAED data. Therefore, the grain size was determined in a range from 220 nm to 290 nm. The number of grains inside the aperture was estimated from SAED patterns in (**Fig. S10**c,d).

For the film of several nanometers, XRD does not provide the sufficient information to resolve the crystal structure, viz., the samples do not exhibit sharp enough peaks in the XRD curves (not shown). Therefore, we conducted selected area electron diffraction in the TEM characterization (**Fig. S11**, **Fig. S12**). The statistics of average grain size was plotted in the histogram (**Fig. S13**).

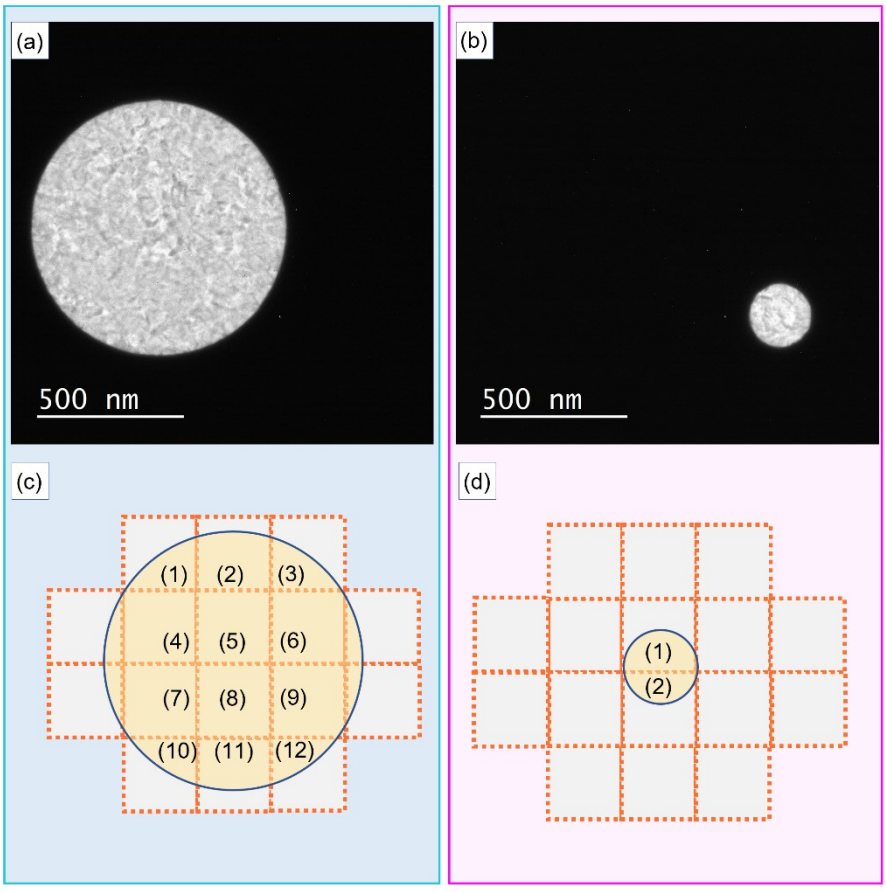


**Fig. S10** Estimation of the grain size of PtS film by the selected area aperture size during the SAED measurement. (a) An aperture size of 860 nm for irradiating the selected area. (b) A smaller aperture size of 220 nm. (c) The larger aperture irradiates twelve grains while the smaller aperture covers the area of (d) two neighboring grains.

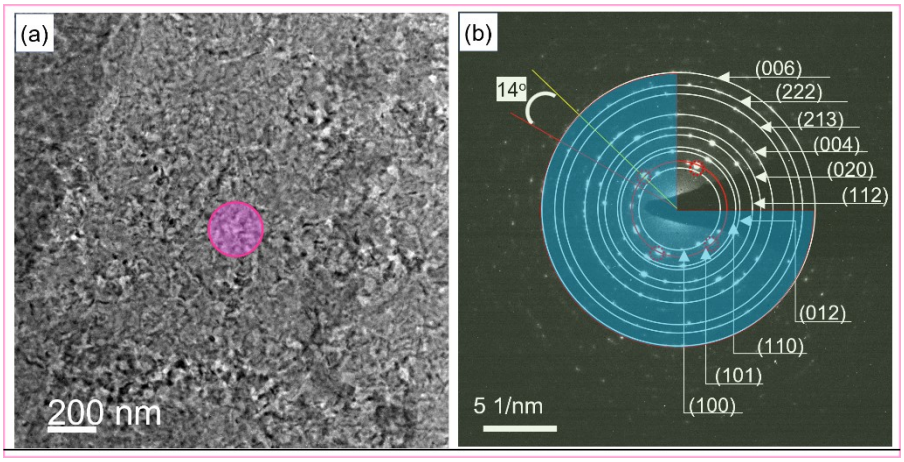


**Fig. S11** SAED pattern of PtS film with a certain selected area. (a) Low magnification TEM graph with a cycle indicating the selected area by an aperture (diameter ca. 220 nm). (b) SAED pattern of the PtS film. The diffraction pattern was assigned with the d spacing of each facet. The (101) facet in red circle was employed for determining the relative rotation of two neighboring grains. The dashed four cycles were used for depicting one set of diffraction. Both radial lines in yellow and red were crossing the spots at (101) ring with indicating two adjacent grains (relative rotation angle ca. 14 °). Here, two was counted for the grain number included in the diffraction pattern.

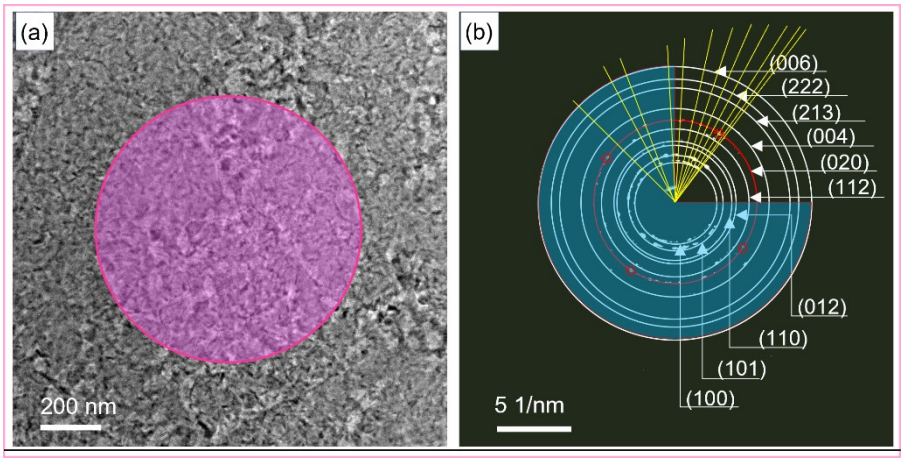


**Fig. S12** SAED pattern of PtS film. (a) Low magnification TEM graph with a cycle showing the selected area by a large aperture (diameter ca. 860 nm). (b) SAED pattern of the PtS film. The diffraction ring was determined with the d spacing of each facet. The (020) facet in red circle was employed for determining the relative rotation of adjacent grains. The dashed four cycles were used for depicting one set of diffraction. The radial lines in yellow were crossing the spots at (020) ring with indicating different grains. Here, twelve was counted for the grain number included in the diffraction pattern.

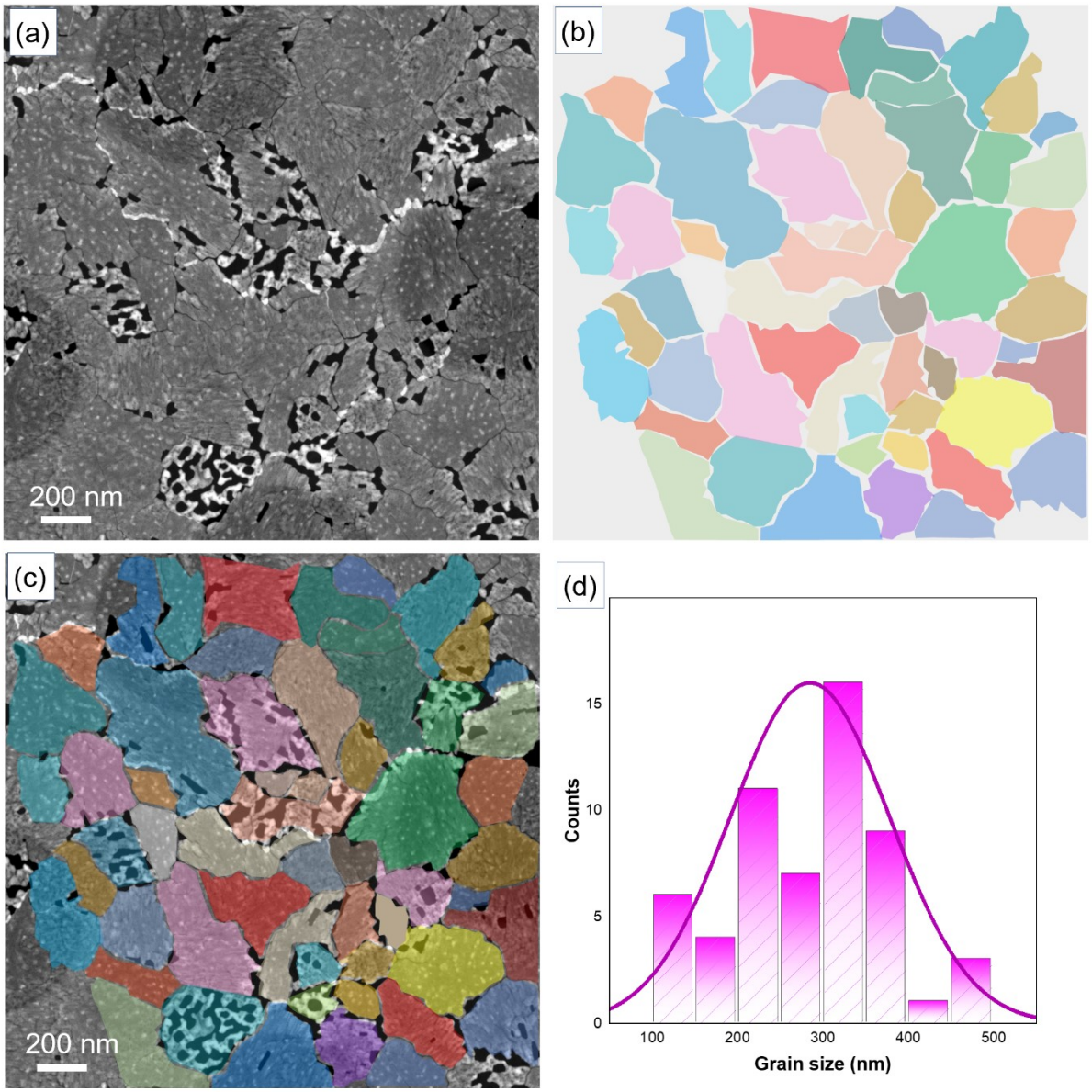


**Fig. S13** Statistics of the average grain size of PtS film. (a) Raw STEM graph of the PtS film. (b) Colored mask for the different neighboring grains. The adjacent grains were determined by the contrast of each grain as well as clear grain boundaries. (c) Fake-color enhanced STEM graph of PtS film. (d) Histogram of the average grain size.

## 3. Thermodynamic calculation of the Gibbs free energy for the PtS and $PtS_2$

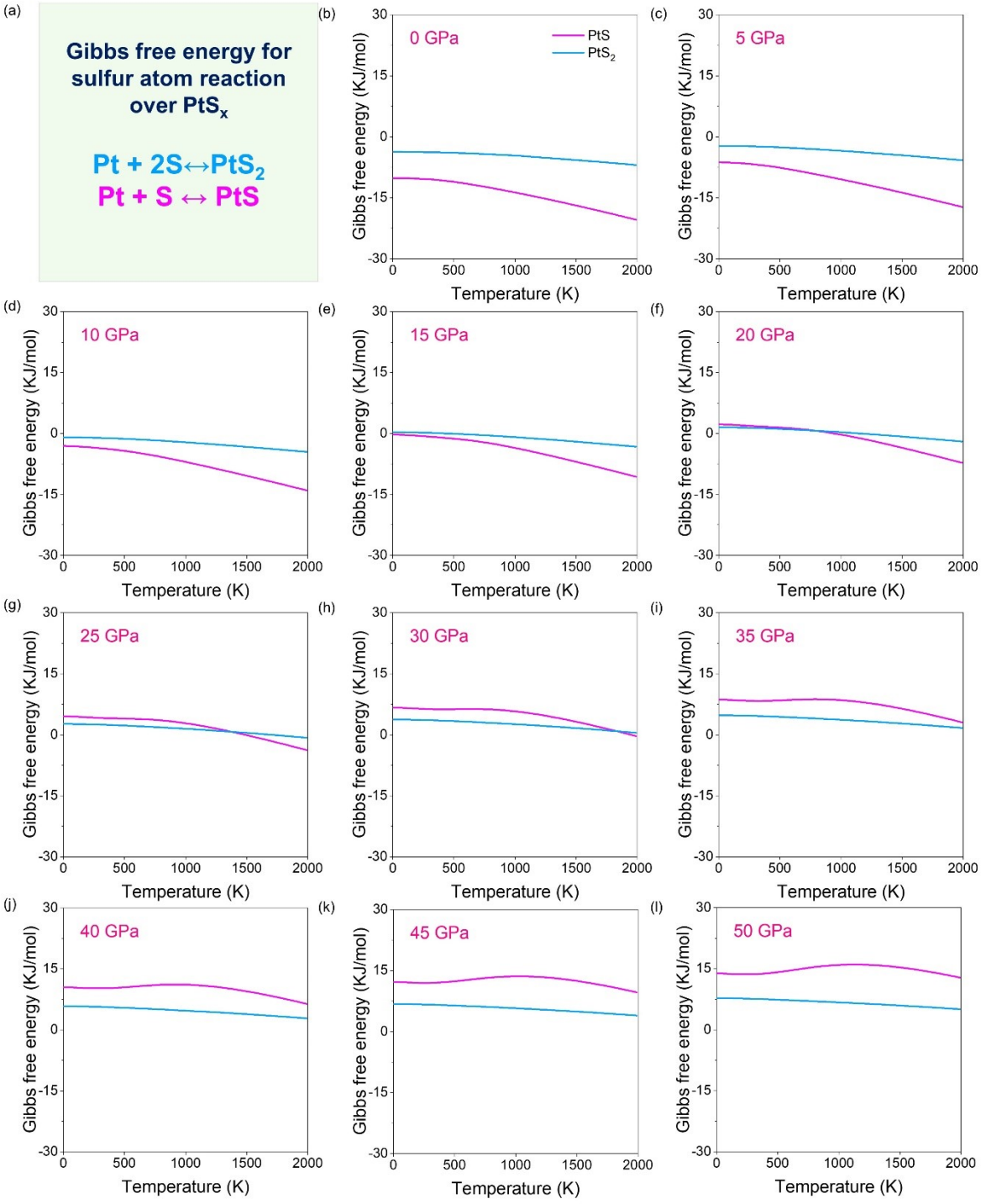


**Fig. S14** Calculated Gibbs free energy of the formation reaction of platinum sulfides including PtS and $PtS_2$. (a) The chemical reaction formula for synthesis of PtS and $PtS_2$. The synthetic reaction occurs at different growth temperature *T* and different pressure *P*. (b-l) The growth pressure was set ranging from 0 GPa 80 GPa. The temperature was set from 0 K to 2000 K.

## 4. Characterization of PtS films of different thickness

The photographs, optical micrographs and Raman spectra of different PtS films (**Fig. S15**) were presented. Besides, the Raman mapping data of PtS film (as integrated in **Fig. 4**c ) shows homogeneity over a large area.

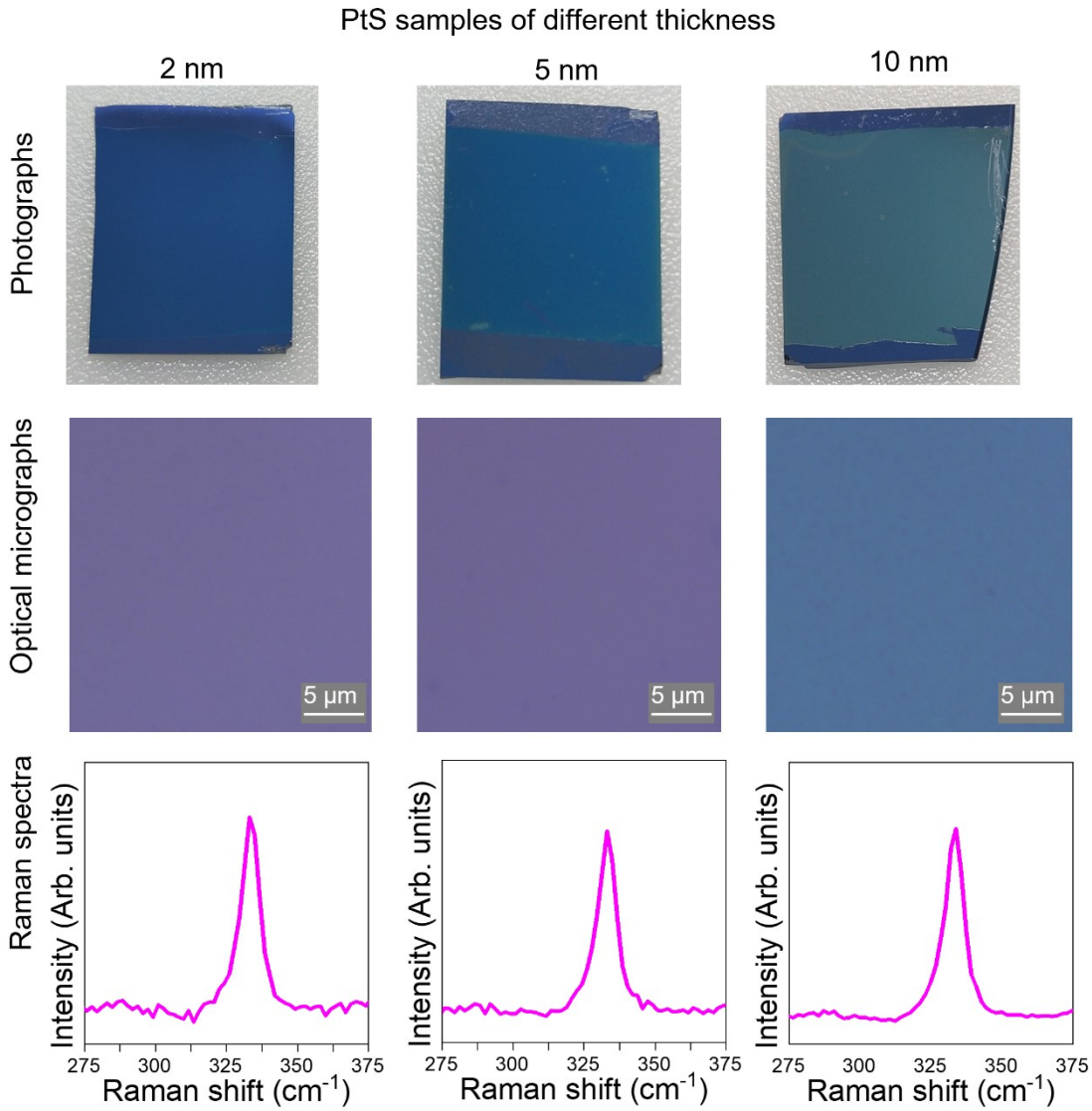


**Fig. S15** The photographs, optical micrographs and Raman spectra of PtS films of different thickness. The typical area of the substrates is 1.5 × 2 $cm^2$. The $B_{1g}$ mode is dominant in the Raman spectra of these PtS samples.

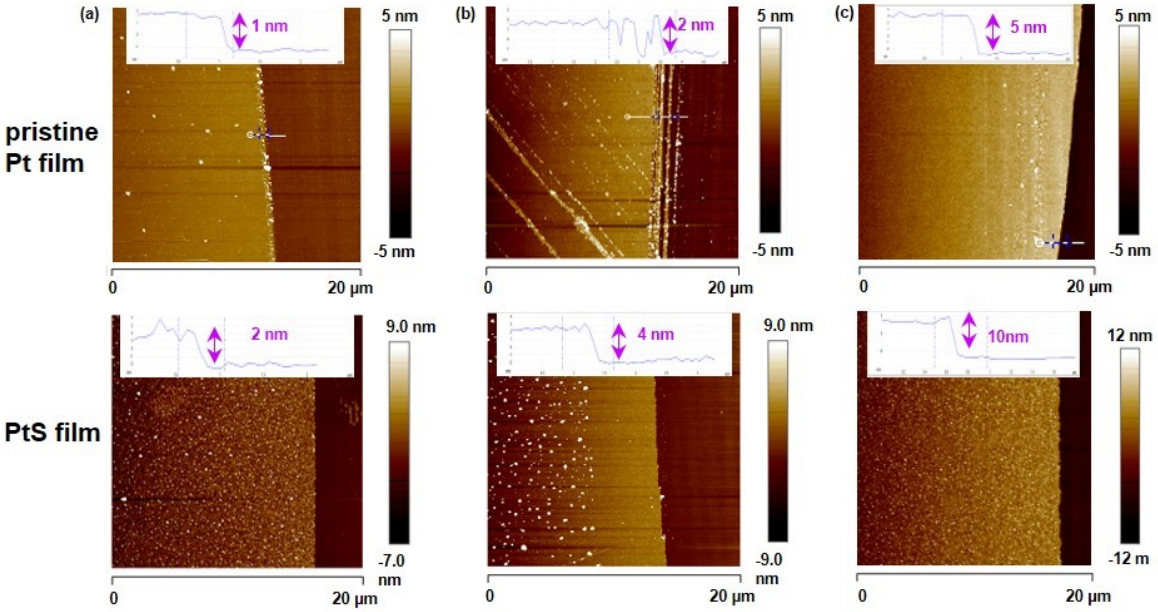


**Fig. S16** AFM graphs for determining the thickness of Pt and PtS films. (a-c) pristine Pt film of different thickness including 1, 2, and 5 nm, respectively. (d-f) the synthetic PtS films with the thickness of 2, 4, and 10 nm, respectively. The roughness was listed in **Table S1** based on the root mean square of the height mapping in the AFM images.

**Table S1**. The surface roughness of the Pt film and PtS film (after sulfurization of Pt)

| Sample list (PtS thickness) | RMS of Pt film (before sulfurization) (nm) | RMS of PtS film (after sulfurization) (nm) |
|---|---|---|
| 2 nm | 0.65 | 0.52 |
| 4 nm | 0.36 | 0.61 |
| 10 nm | 0.42 | 0.78 |

## 5. Performances of PtS based photodetectors.

### Device performances of PtS based photodetectors.

The responsivity and detectivity of a typical PtS based device (**Fig. S17**a) is 201 mA $W^{-1}$ and $5.3\times10^{9}$ Jones, respectively. The rise and decay time of PtS photodetector (**Fig. S17**b) are 0.29 s and 0.82 s, respectively. Here, the 650 nm laser possesses a full power of 186 mW (calibrated by a light power meter). The biased voltage was set as 4.5 V.

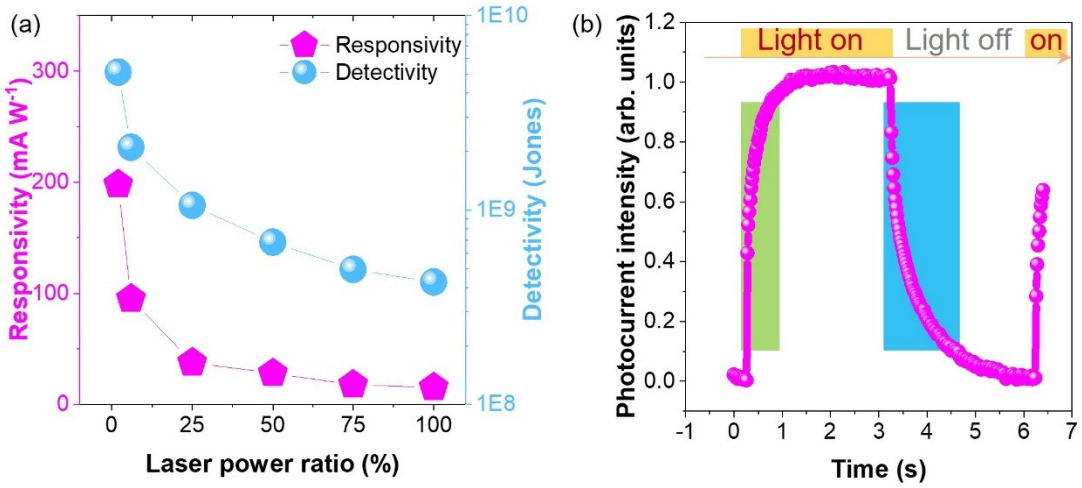


**Fig. S17** The device performances of the PtS based photodetector. (a) Responsivity and detectivity of the device. (b) Rise and decay time of the device.

We have collected the absorption spectrum of the PtS film. We also evaluated other wavelengths by taking 405 and 532 nm as examples. These data were attached as follows.

It is not straightforward to measure the absorbance spectra of the PtS film directly grown on $Si/SiO_2$ substrate. Therefore, we synthesized the PtS film on (transparent) quartz substrate to collect the absorbance spectra. The absorption spectra of PtS film were presented in **Fig. S18** and the photocurrent response of PtS photodetectors under different-wavelength lasers are demonstrated (**Fig. S19).**

The following are the optical absorbance spectra of PtS films and their photocurrent response upon illumination by light of different wavelength.

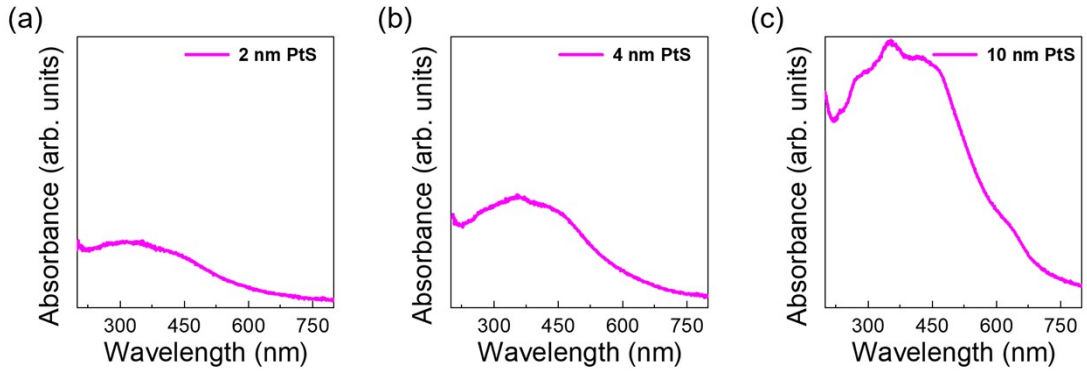


**Fig. S18** The absorbance spectra of the PtS film.

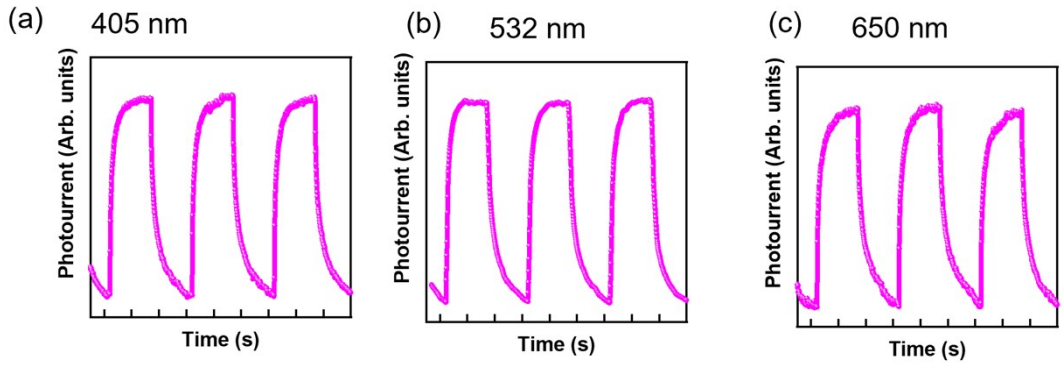


**Fig. S19** The photocurrent response curves of the PtS film under the illumination of light of different wavelength.

## References


1. P. Y. Huang, C. S. Ruiz-Vargas, A. M. van der Zande, W. S. Whitney, M. P. Levendorf, J. W. Kevek, S. Garg, J. S. Alden, C. J. Hustedt, Y. Zhu, J. Park, P. L. McEuen and D. A. Muller, *Nature*, 2011, **469**, 389-392.
2. A. M. van der Zande, P. Y. Huang, D. A. Chenet, T. C. Berkelbach, Y. You, G. H. Lee, T. F. Heinz, D. R. Reichman, D. A. Muller and J. C. Hone, *Nat. Mater.*, 2013, **12**, 554-561.
3. M. P. Levendorf, C. J. Kim, L. Brown, P. Y. Huang, R. W. Havener, D. A. Muller and J. Park, *Nature*, 2012, **488**, 627-632.
4. J. Pang, R. G. Mendes, P. S. Wrobel, M. D. Wlodarski, H. Q. Ta, L. Zhao, L. Giebeler, B. Trzebicka, T. Gemming, L. Fu, Z. Liu, J. Eckert, A. Bachmatiuk and M. H. Rummeli, *ACS Nano*, 2017, **11**, 1946-1956.
5. D. Wu, C. Jia, F. Shi, L. Zeng, P. Lin, L. Dong, Z. Shi, Y. Tian, X. Li and J. Jie, *J. Mater. Chem. A*, 2020, **8**, 3632-3642.
6. D. Wu, J. Guo, J. Du, C. Xia, L. Zeng, Y. Tian, Z. Shi, Y. Tian, X. J. Li, Y. H. Tsang and J. Jie, *ACS Nano*, 2019, **13**, 9907-9917.
7. X. M. Li, D. J. Yu, F. Cao, Y. Gu, Y. Wei, Y. Wu, J. Z. Song and H. B. Zeng, *Adv. Funct. Mater.*, 2016, **26**, 5903-5912.
8. D. Zhang, C. Liu, K. Li, W. Guo, F. Gao, J. Zhou, X. Zhang and S. Ruan, *Adv. Opt. Mater.*, 2018, **6**, 1701189.
9. G. Kresse and J. Furthmuller, *Phys. Rev. B*, 1996, **54**, 11169-11186.
10. G. Kresse and J. Furthmüller, *Comput. Mater. Sci.*, 1996, **6**, 15-50.
11. J. P. Perdew, K. Burke and M. Ernzerhof, *Phys. Rev. Lett.*, 1996, **77**, 3865-3868.
12. G. Kresse and D. Joubert, *Phys. Rev. B*, 1999, **59**, 1758-1775.
13. P. E. Blöchl, *Phys. Rev. B*, 1994, **50**, 17953-17979.
14. H. J. Monkhorst and J. D. Pack, *Phys. Rev. B*, 1976, **13**, 5188-5192.
15. M. V. Bollinger, K. W. Jacobsen and J. K. Nørskov, *Phys. Rev. B*, 2003, **67**, 5410.
16. P. J. Linstrom and W. G. Mallard, *NIST Chem. WebBook*, 2018, **1**,

DOI:10.18434/T18434D18303.